

Article

# Synthesis of Self-Supported Cu/Cu<sub>3</sub>P Nanoarrays as an Efficient Electrocatalyst for the Hydrogen Evolution Reaction

Rui Dang <sup>1,\*</sup> , Xiufeng Xu <sup>2</sup>, Mengmeng Xie <sup>2</sup> and Jian Liu <sup>2,\*</sup><sup>1</sup> Northwest Institute for Nonferrous Metal Research, 96 Weiyang Road, Weiyang District, Xi'an 710016, China<sup>2</sup> Faculty of Printing, Packaging Engineering and Digital Media Technology, Xi'an University of Technology, Xi'an 710054, China; xfengalone@163.com (X.X.); xiemeng1216@163.com (M.X.)

\* Correspondence: dr0501@163.com (R.D.); liujian@xaut.edu.cn (J.L.)

**Abstract:** Owing to the energy crisis and environmental pollution, it is essential to develop cheap, environmentally friendly and sustainable energy to replace noble metal electrocatalysts for use in the hydrogen evolution reaction (HER). We report herein that a Cu/Cu<sub>3</sub>P nanoarray catalyst was directly grown on the surfaces of Cu nanosheets from its Cu/CuO nanoarray precursor by a low-temperature phosphidation process. In particular, the effects of phosphating distance, mass ratio and temperature on the morphology of Cu/Cu<sub>3</sub>P nanoarrays were studied in detail. This nanoarray, as an electrocatalyst, displays excellent catalytic performance and long-term stability in an acid solution for electrochemical hydrogen generation. Specifically, the Cu/Cu<sub>3</sub>P nanoarray-270 exhibits a low onset overpotential (96 mV) and a small Tafel slope (131 mV dec<sup>-1</sup>).

**Keywords:** Cu/Cu<sub>3</sub>P nanoarrays; Cu nano-substrates; electrocatalyst; HER



**Citation:** Dang, R.; Xu, X.; Xie, M.; Liu, J. Synthesis of Self-Supported Cu/Cu<sub>3</sub>P Nanoarrays as an Efficient Electrocatalyst for the Hydrogen Evolution Reaction. *Catalysts* **2022**, *12*, 762. <https://doi.org/10.3390/catal12070762>

Academic Editors: Yongjun Ji, Liwen Xing and Ke Wu

Received: 27 May 2022

Accepted: 7 July 2022

Published: 9 July 2022

**Publisher's Note:** MDPI stays neutral with regard to jurisdictional claims in published maps and institutional affiliations.



**Copyright:** © 2022 by the authors. Licensee MDPI, Basel, Switzerland. This article is an open access article distributed under the terms and conditions of the Creative Commons Attribution (CC BY) license (<https://creativecommons.org/licenses/by/4.0/>).

## 1. Introduction

Due to the excessive consumption of fossil fuels, the resulting environmental pollution and global energy crisis have aroused widespread concern. It is essential to develop clean, environmental friendly and renewable energy sources to reduce our dependence on fossil fuels and benefit the environment by reducing greenhouse gas emissions [1–7]. Among variable alternatives, hydrogen has been considered as an ideal energy carrier due to its environmental friendliness and high energy density. Electrochemical water splitting is one of the most simple and promising strategies to create high-purity hydrogen in an economic way [8–14]. However, the production efficiency is low without the use of electrocatalysts, which can significantly reduce the large overpotential for the hydrogen evolution reaction (HER). It is well known that Pt, Ru-based and Ir-based catalysts are regarded as the most promising electrocatalysts for the HER and OER, because of their high electrocatalytic performance [15–23], whereas their widespread application is restricted by their high costs and low abundance on Earth. Therefore, the major challenge in hydrogen production is to reduce the use of noble metals or replace them with inexpensive non-precious metal catalysts.

In recent years, a lot of effort in the field of highly active, Earth-abundant catalysts has been dedicated to various types of alternative materials, such as transition metal sulfides [24–26], metal carbides [27–29], metal nitrides [30–32], metal phosphides [33–36] and even metal-free materials [37,38]. Transition-metal phosphides (TMPs) are an important class of compounds with metalloid characteristics and good electrical conductivity. In the structure of metal phosphides, negatively charged P atoms can act as ideal active centers for proton adsorption, bringing about the dynamical optimization of the HER [39–41]. To date, various metal phosphides have been adopted for electrochemical hydrogen evolution, such as cobalt phosphide nanoparticles (CoP NPs [42]), nickel phosphide nanoparticles (Ni<sub>2</sub>P NPs [43]), molybdenum phosphide nanoparticles (MoP NPs [44]) and Ni-Fe phosphide nano hybrids [45], which have attracted attention for their excellent electrocatalytic activities

for the HER. However, the relatively low electrical conductivity of most phosphide catalysts remains a problem, leading to limited charge transfer and passivated electrocatalytic activity. Furthermore, these electrocatalysts are prone to agglomeration under high current density or long-term tests in practical application in the HER.

To overcome the above-mentioned issues, alternative architectural arrays grown on conductive substrates have been explored due to the large surface area, abundant active sites, and synergistic effects between the electrocatalysts and the conductive substrates. Recently, Sun and co-workers [46] reported on porous urchin-like Ni<sub>2</sub>P microsphere superstructures anchored on nickel foam, which afforded a current density of 10 mA cm<sup>-2</sup> at a low overpotential of only -98 mV for the HER. Tan and co-workers [47] reported on flower-like structures consisting of NiCoP-CoP nanowires grown directly on porous nickel frameworks to achieve a highly efficient HER in an alkaline solution. For the HER, a binder-free NiCoP-CoP/Ni/NF electrode can reach 10 mA cm<sup>-2</sup> current density at a quite low overpotential of 49 mV. Despite extensive progress in nanoarray architectures, self-supporting nanoarray structures on conductive materials are still a key challenge.

Over the past decade, Fe, Co and Ni as electrocatalysts have exhibited excellent catalytic performance for the HER. Nevertheless, as an Earth-abundant transition metal, Cu-based catalysts have been relatively less studied in terms of the HER. Therefore, it is significant to design Cu-based materials with special structures for developing high-efficiency electrocatalysts. Recent studies have shown that Cu<sub>3</sub>P is an excellent electrocatalyst for use in the HER [48,49]. Herein, self-supported Cu/Cu<sub>3</sub>P nanoarrays were successfully grown on the surfaces of Cu nanosheets from Cu/CuO nanoarrays precursor by a low-temperature phosphidation process. The Cu/Cu<sub>3</sub>P nanoarray-270, as an electrocatalyst, displays excellent catalytic performance and durability for electrochemical hydrogen generation, and exhibits a low onset overpotential (96 mV) and a small Tafel slope (131 mV dec<sup>-1</sup>). The morphology and nanostructure of the self-supported Cu/Cu<sub>3</sub>P nanoarray catalyst affect the electrocatalytic efficiency significantly. The nanoarrays possess large surface areas and a great number of active sites, which is immensely beneficial for electrocatalysis capacity enhancement. At the same time, copper-based catalysts can also be used in other types of organic reactions [50]. It is expected that this innovative approach will become a new concept to synthesize highly efficient catalysts.

## 2. Results

The typical procedure for the synthesis of Cu/Cu<sub>3</sub>P nanoarrays is summarized in Figure 1. In brief, Cu nanosheets are firstly synthesized according to hydrothermal method. Then, Cu nanosheets, as both a self-template and nano-conductive substrate, are immersed in a solution of NaOH/H<sub>2</sub>O<sub>2</sub> for the formation of Cu/CuO nanoarrays. Cu/CuO nanoarrays and NaH<sub>2</sub>PO<sub>2</sub> are calcinated under an Ar gas flow; the original black color of the Cu/CuO turns gray after the phosphorization process, thus suggesting that the copper oxides on the surfaces of Cu nanosheets are converted into cuprous phosphide.

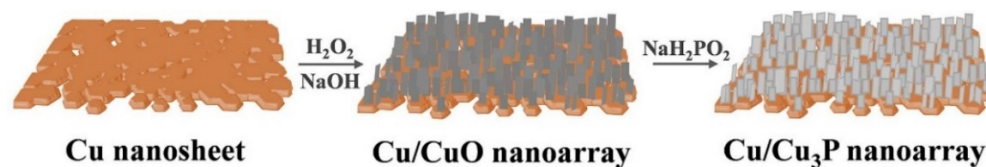
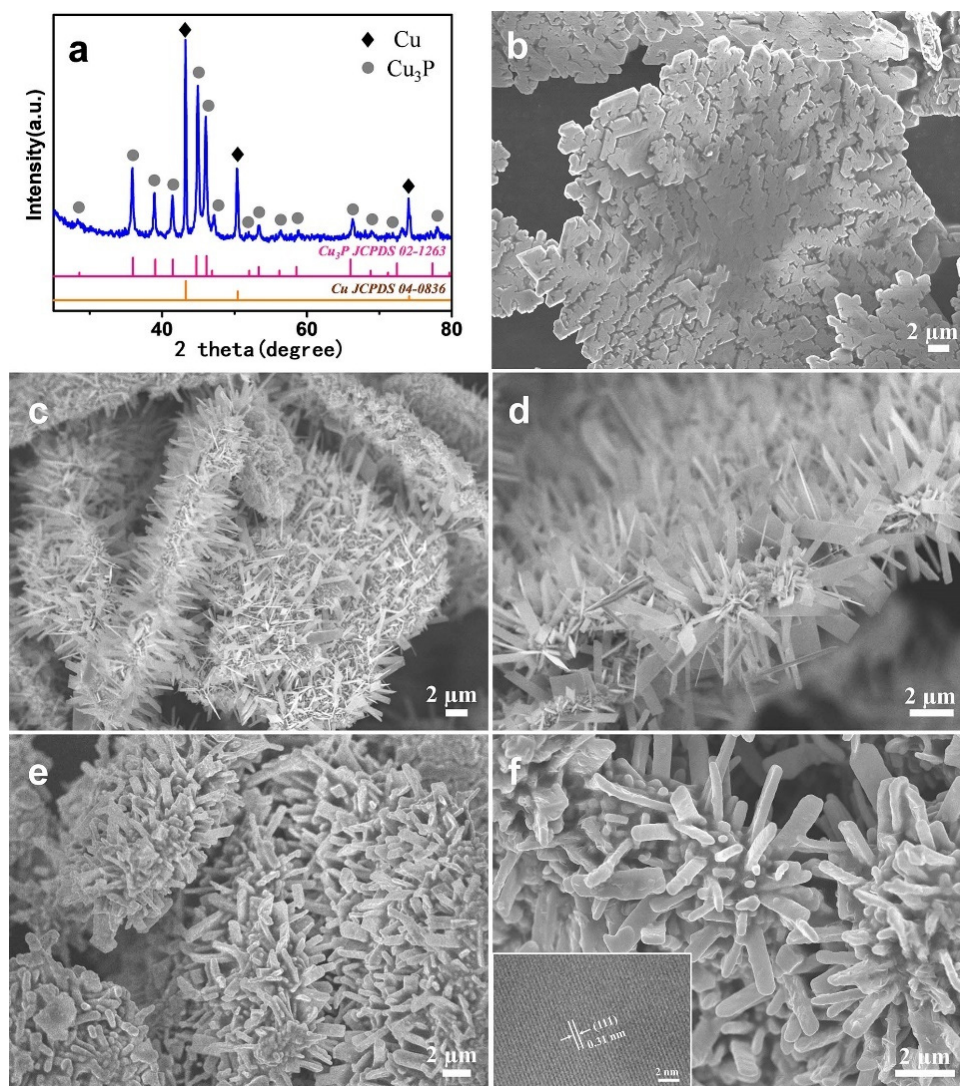


Figure 1. Illustration of the preparation of Cu/Cu<sub>3</sub>P nanoarrays.

The X-ray diffraction (XRD) patterns of the Cu/CuO nanoarrays before and after phosphidation are shown in Supplementary Figures S1c and 2a. The precursor shows diffraction peaks characteristic of CuO (JCPDS No. 04-1548). In contrast, only peaks corresponding to Cu<sub>3</sub>P can be observed for the resulting copper phosphide. Figure 2a shows that all diffraction peaks are in accordance with the hexagonal structure of Cu<sub>3</sub>P (JCPDS No. 02-1623), and the strong peaks at 43.4°, 50.4° and 74.1° originate from the Cu nanosheets (JCPDS No. 04-0836), indicating that all copper oxides are completely trans-

formed into cuprous phosphides in the phosphating process, while the copper nanosheets, as a conductive template, have not been completely consumed.



**Figure 2.** Characterization of the morphology and structure of sample: (a) XRD pattern of Cu/Cu<sub>3</sub>P nanoarrays. (b) SEM image of Cu nanosheets. (c,d) SEM images of Cu/CuO nanoarrays. (e,f) SEM images of Cu/Cu<sub>3</sub>P nanoarrays; inset shows the HRTEM of Cu<sub>3</sub>P.

The morphologies of products were characterized by scanning electron microscopy (SEM). Figures 2b and S1a show the SEM images of Cu nanosheets as the self-template and conductive substrate, which had a large area of 30–100  $\mu\text{m}$  in diameter with smooth surface. The SEM images of the Cu/CuO nanoarrays at different magnification are shown in Figures 2c,d and S2. The CuO nanoarrays are uniformly distributed on the surface of the Cu nanosheet, consisting of uniform nanoplates with a width ranging from 30 nm to 80 nm and are 3–5  $\mu\text{m}$  in length. After phosphidation, the nanoarray morphology is still preserved, as shown in Figure 2e,f. The plate Cu<sub>3</sub>P nanoarrays grown on the Cu nanosheet substrate and the surfaces of the nanoarrays become rough. The high-magnification SEM image of the Cu<sub>3</sub>P nanoplate is shown in Figure S3, and close observation reveals that the thickness of an individual Cu<sub>3</sub>P nanoplate increases from 60 nm to 120 nm in the phosphating process. The nanoarray structure helps to expose more active sites in the catalytic reaction, and the interspace between the nanoarrays can favor the diffusion of electrolytes. The high-resolution transmission electron microscopy (HRTEM) image (inset f) shows clear lattice fringes with an interplane distance of 0.31 nm, corresponding to the

(111) of the  $\text{Cu}_3\text{P}$ . All these results clearly confirm the successful synthesis of  $\text{Cu}/\text{Cu}_3\text{P}$  nanoarrays by low-temperature phosphidation from the  $\text{Cu}/\text{CuO}$  nanoarray precursor.

The detailed elemental compositions and valence states of as-synthesized  $\text{Cu}/\text{Cu}_3\text{P}$  were characterized by X-ray photoelectron spectroscopy (XPS), as shown in Figure 3. The full survey XPS spectrum (Figure S4) shows that the  $\text{Cu}/\text{Cu}_3\text{P}$  comprises Cu, P, O and C elements. As shown in Figure 3a, two main peaks of Cu 2p are located at 934.6 eV and 954.4 eV, which represent the Cu  $2p_{3/2}$  and Cu  $2p_{1/2}$  peaks, respectively. The peaks at 933.1 eV and 935.1 eV are assigned to the  $\text{Cu}^{\delta+}$  in the  $\text{Cu}_3\text{P}$  and oxidized Cu for the Cu  $2p_{3/2}$  energy level, while the peaks at 940.8 and 944.1 eV belong to the satellite peaks of Cu  $2p_{3/2}$ . The three peaks appearing at 952.8, 955.2 and 962.9 eV are indexed to the  $\text{Cu}^{\delta+}$  in the  $\text{Cu}_3\text{P}$ , oxidized Cu and the satellite for Cu  $2p_{1/2}$ , respectively [51,52]. In Figure 3b, the peak at 133.6 eV could be indexed to oxidized phosphate species, resulting from the exposure of the sample to air. The lower binding energy peaks situated at around 129.1 eV and 129.9 eV correspond to P  $2p_{3/2}$  and P  $2p_{1/2}$  of  $\text{Cu}/\text{Cu}_3\text{P}$  nanoarrays, respectively [53,54]. Note that the binding energy of P 2p (129.9 eV) shows a negative shift from elemental P (130.2 eV), indicating that P carries a negative charge ( $\delta^-$ ). The results suggest that charge transfer occurs between Cu and P, in which Cu may serve as the hydride-acceptor center and P may act as the proton-acceptor center [55].

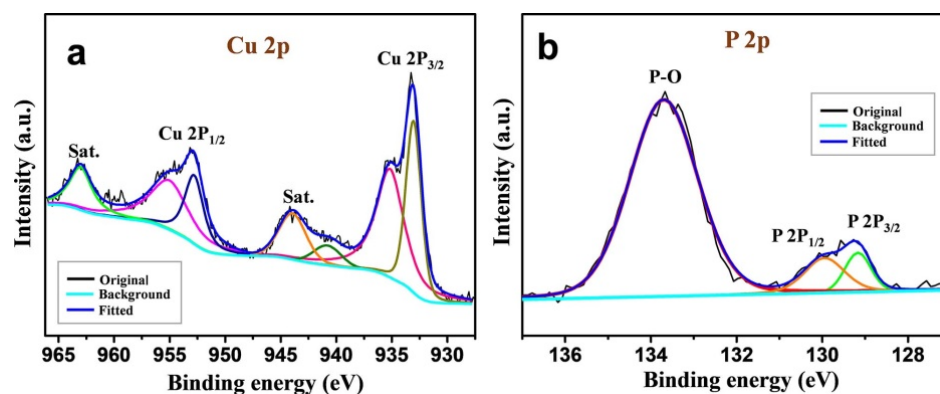
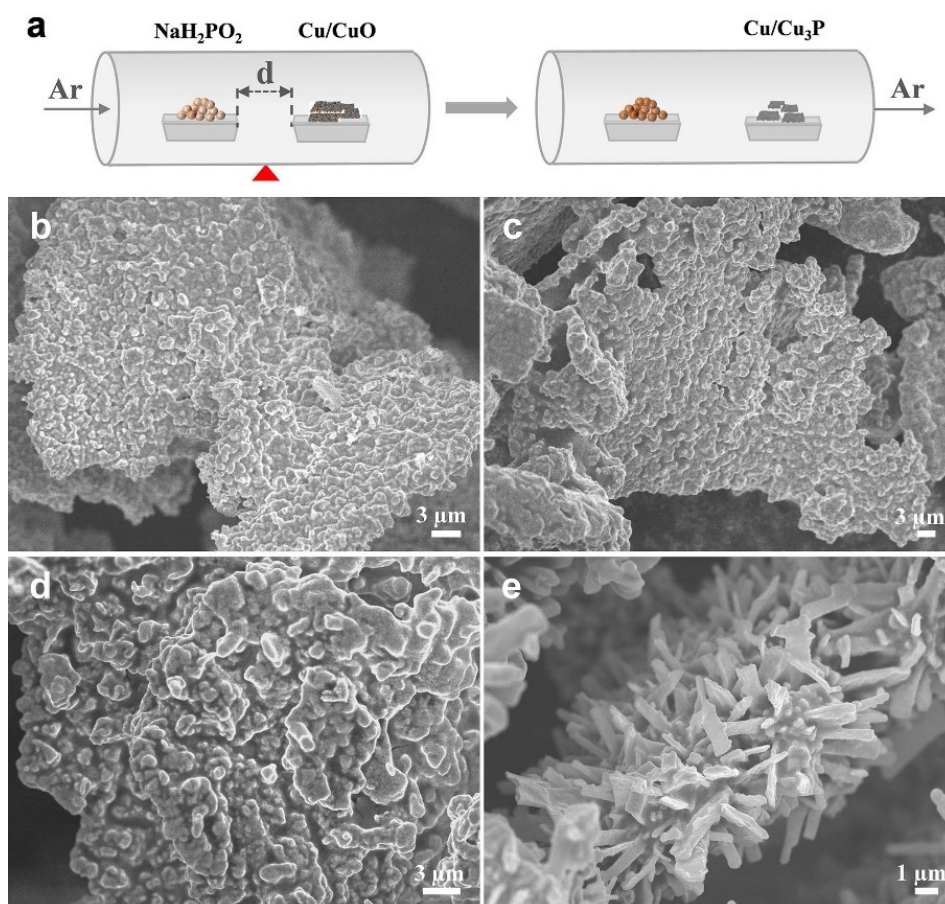


Figure 3. Cu 2p (a) and P 2p (b) core-level spectra of  $\text{Cu}/\text{Cu}_3\text{P}$  nanoarrays.

The fabrication process of the  $\text{Cu}/\text{Cu}_3\text{P}$  nanoarray is illustrated in Figure 4a. The morphology of the products was found to strongly depend on the distance between  $\text{Cu}/\text{CuO}$  nanoarrays and sodium hypophosphite in the phosphating process. When the distance between the two precursors is less than 5 cm, the nanoarray structure on the surface of the Cu nanosheets disappears and its surface becomes rough, as shown in Figure 4b,c. Further increasing the phosphating distance to 16 cm, part of the array structure on the surface can be observed, as shown in Figure 4d. The nanoarrays are obviously thicker than the original  $\text{CuO}$  nanoplate, and agglomeration between the nanoarrays is more serious. When the phosphating distance was extended to 24 cm (in Figure 4e), the nanoarray structure composed of  $\text{Cu}_3\text{P}$  nanoplates with a width of around 300–800 nm and lengths of up to several micrometers was vertically grown on the surface of the Cu nanosheets. The topotactic conversion of the  $\text{Cu}/\text{CuO}$  nanoarrays into the  $\text{Cu}/\text{Cu}_3\text{P}$  nanoarray could be explained as follows: first, the thermal decomposition of  $\text{NaH}_2\text{PO}_2$  generates  $\text{PH}_3$ , and the  $\text{CuO}$  nanoarrays are reduced to Cu nanoarrays by  $\text{PH}_3$ . Then, the resulting Cu subsequently catalyzes the decomposition of  $\text{PH}_3$  into elemental P. Finally, the elemental P further reacts with Cu to form  $\text{Cu}_3\text{P}$  nanoarrays.

The influence of different mass ratios of phosphorus precursor and the  $\text{Cu}/\text{CuO}$  nanoarrays on the morphology and crystal structure was investigated, as shown in Figure 5. When the mass ratio of  $\text{NaH}_2\text{PO}_2$  to  $\text{CuO}$  is 1, the morphology of  $\text{Cu}/\text{Cu}_3\text{P}$  nanoarrays does not change significantly (Figure 5a), and the corresponding XRD pattern shows that only a small amount of  $\text{Cu}_3\text{P}$  is formed in the product (Figure 5b), indicating that the  $\text{CuO}$  cannot be converted into  $\text{Cu}_3\text{P}$  at this ratio. When the mass ratio of  $\text{NaH}_2\text{PO}_2/\text{CuO}$  increases to

2, the obtained array structure is thicker than that of the precursor (Figure 5c), and the corresponding XRD pattern reveals that CuO has been converted into Cu<sub>3</sub>P completely, but the amount of Cu<sub>3</sub>P in the product is small (Figure 5d). When the mass ratio of NaH<sub>2</sub>PO<sub>2</sub>/CuO further increases to 2.5, the morphology of the product still maintains the nanoarray structure (Figure 5e), and the corresponding XRD pattern shows that Cu<sub>3</sub>P is generated, while the peak intensity of the copper substrate does not change significantly (Figure 5f), indicating that the Cu nanosheet has not been converted. Until the mass ratio of NaH<sub>2</sub>PO<sub>2</sub>/CuO reached 3, the corresponding SEM image of this sample reveals that the Cu<sub>3</sub>P nanoarrays thickened and agglomerated together (Figure 5g). The intensity of the XRD pattern of Cu in the product is significantly weakened (Figure 5h), indicating that the Cu nanosheet substrate is partially converted into Cu<sub>3</sub>P during the phosphating reaction.



**Figure 4.** (a) Schematic of the preparation process of the Cu<sub>3</sub>P nanoarrays via the phosphorization of Cu/CuO. (b–e) SEM images of products at different distances between Cu/CuO and NaH<sub>2</sub>PO<sub>2</sub>: (b)  $d = 0$  cm, (c)  $d = 5$  cm, (d)  $d = 16$  cm and (e)  $d = 24$  cm.

The influence of the phosphating temperature on the nanostructures formed was investigated, as shown in Figure 6. Figure 6a,b show that CuO and Cu<sub>3</sub>P were simultaneously observed on the Cu nanosheets at 260 °C. With the increase in temperature, the thickness of nanoarrays composed of nanoplates was increased, while the CuO nanoarrays were completely converted to Cu<sub>3</sub>P nanoarrays at 290 °C, as shown in Figure 6c,d. Until the temperature reached 310 °C, the nanoarray structures grown on the surfaces of Cu nanosheets experienced obvious agglomeration and collapse, and the corresponding XRD pattern revealed that a part of the Cu nanosheets was converted to Cu<sub>3</sub>P in the phosphating reaction (Figure 6e,f). The effects of phosphating time on the morphology and phase of as-prepared nanostructures were likewise studied, as shown in Figure S5. When the calcination time was increased to 1.5 h, the morphology of the product obtained was as shown

in Figure S5c. The nanoarray structure composed of nanoplates is significantly thicker than that obtained at 1 h (Figure S5a). Moreover, the weak diffraction peak of Cu indicated that most of the Cu nanosheet substrates were transformed into  $\text{Cu}_3\text{P}$  (Figure S5d). The above results reveal that the phosphating temperature and time had a great impact on the formation of the resultant Cu/ $\text{Cu}_3\text{P}$  nanoarrays in the present study.

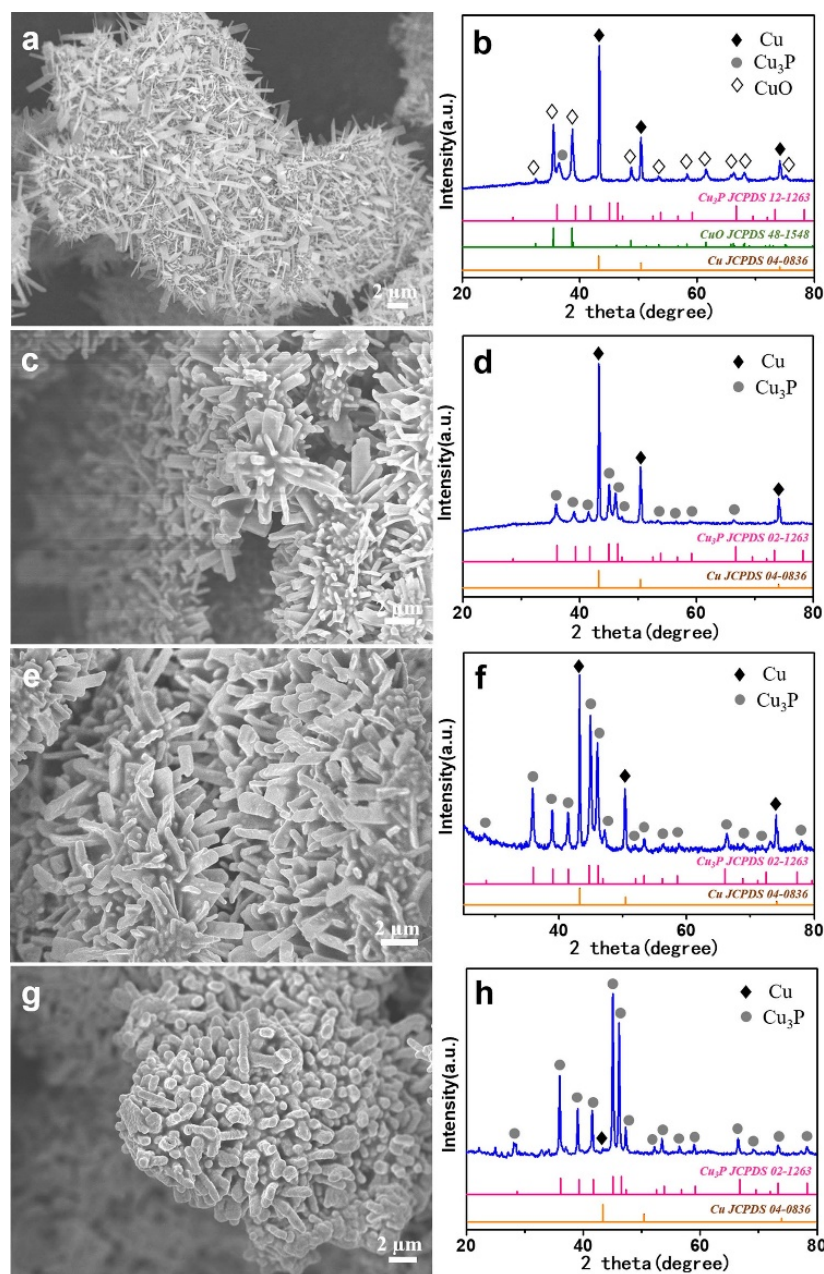


**Figure 5.** SEM images and XRD patterns of products at different mass ratios of  $\text{NaH}_2\text{PO}_2/\text{CuO}$ : (a,b) 1, (c,d) 2, (e,f) 2.5, (g,h) 3.

As a comparison, the pure Cu nanosheet was directly phosphated and calcined under the same conditions, while the morphology and crystal structure of the products were characterized. As shown in Figure S6a, the 2D nanosheet morphology was still preserved, and the smooth surface of the Cu nanosheets became rough after phosphating. At the same time, the corresponding XRD pattern confirmed that  $\text{Cu}_3\text{P}$  was indeed generated (Figure S6b). The results indicate that the CuO nanoarray on the surface of the Cu nanosheet plays a very significant role in maintaining the morphology of Cu/ $\text{Cu}_3\text{P}$  nanoarrays.

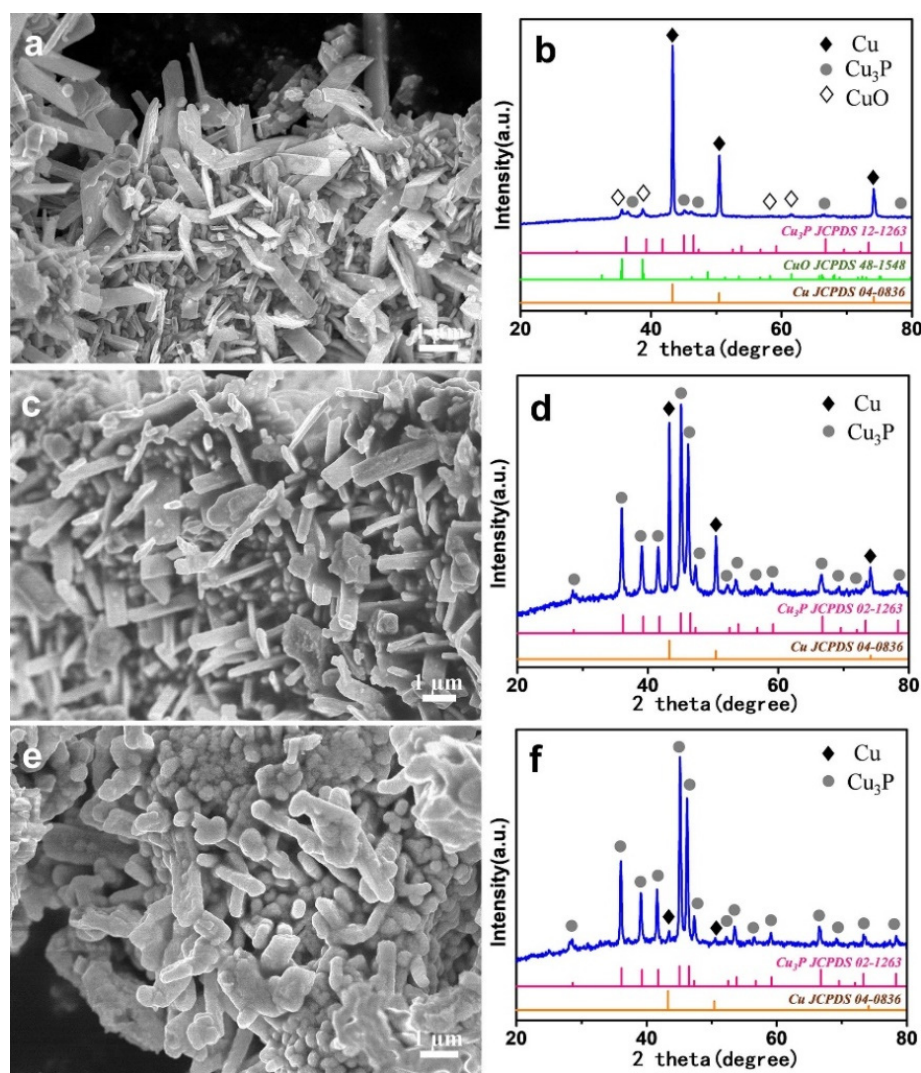


**Figure 6.** SEM images and XRD patterns of products at different phosphating temperatures: (a,b) 260 °C, (c,d) 290 °C, (e,f) 310 °C.

The electrocatalytic activity of the Cu/Cu<sub>3</sub>P nanoarray for the HER was tested by using a standard three-electrode device in 0.5 M H<sub>2</sub>SO<sub>4</sub> solution. Figure 7 shows the polarization curves of these electrodes obtained at different temperatures without iR correction. The catalytic behavior of Cu/Cu<sub>3</sub>P NS obtained by the direct phosphating of the Cu nanosheet was also investigated for comparison. Obviously, the Cu/Cu<sub>3</sub>P NS showed poor electrocatalytic activity, with an onset overpotential value of 347 mV. In sharp contrast, Cu/Cu<sub>3</sub>P nanoarray-270 was significantly active for the HER, with an onset overpotential as low as 96 mV, and additional negative potential leads to a rapid rise in the cathodic current. It requires 253 mV of overpotential ( $\eta_{10}$ ) to reach a current density ( $j$ ) of 10 mA cm<sup>-2</sup>, which is lower than that of Cu/Cu<sub>3</sub>P nanoarray-290 ( $\eta_{10}$  = 342 mV) and Cu/Cu<sub>3</sub>P nanoarray-310 ( $\eta_{10}$  = 395 mV). Moreover, an overpotential of 424 mV is required for Cu/Cu<sub>3</sub>P nanoarray-270 to reach the current density of 100 mA cm<sup>-2</sup>, which is much lower than that of Cu/Cu<sub>3</sub>P nanoarray-290 ( $\eta_{100}$  = 589 mV) and Cu/Cu<sub>3</sub>P nanoarray-310 ( $\eta_{100}$  = 635 mV).

The Tafel slope is an effective means to assess the advantages of electrocatalysts. The Tafel plots in Figure 7b were obtained from the linear portion that conformed to the Tafel equation ( $\eta = a + b \log j$ , where  $b$  is the Tafel slope and  $j$  is the current density). It can be seen that the Tafel slope for Cu/Cu<sub>3</sub>P nanoarray-270 is 131 mV dec<sup>-1</sup>, much lower than that of Cu/Cu<sub>3</sub>P nanoarray-290 (145 mV dec<sup>-1</sup>) and Cu/Cu<sub>3</sub>P nanoarray-310 (156 mV dec<sup>-1</sup>).

These results indicate that Cu/Cu<sub>3</sub>P nanoarray-270 exhibits high electrocatalytic efficiency. A detailed comparison of Cu/Cu<sub>3</sub>P nanoarray-270 with other electrocatalysts is shown in Table S1, indicating its superior or comparable performance [56–59].

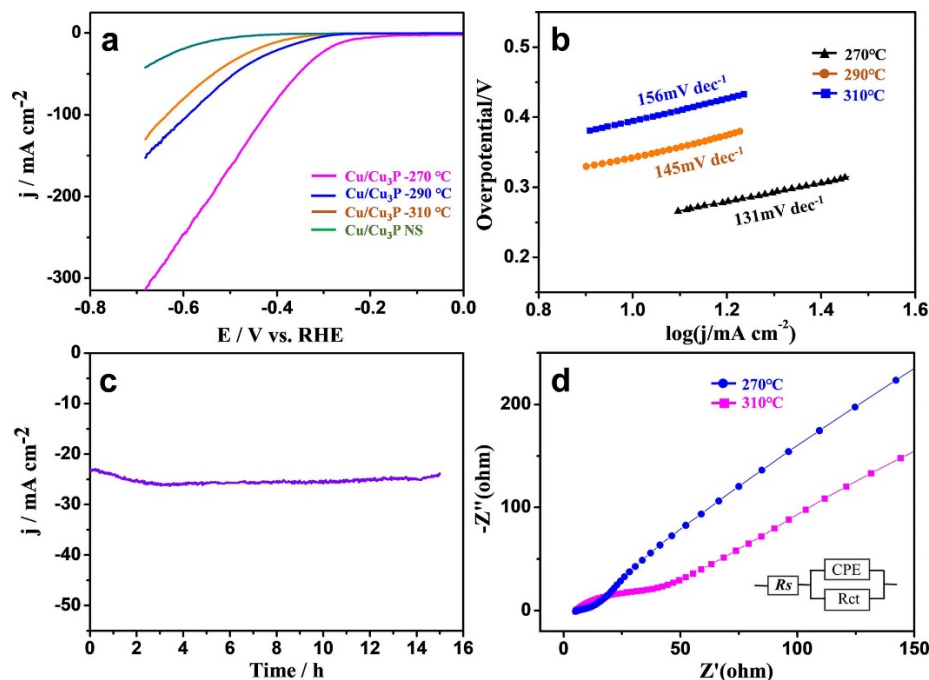


**Figure 7.** Electrocatalytic activity of the as-prepared Cu/Cu<sub>3</sub>P nanoarray electrode for HER in 0.5 M H<sub>2</sub>SO<sub>4</sub>. (a) Polarization curves, (b) Tafel plots, (c) EIS Nyquist plots (inset: the equivalent circuit), (d) current density curve related to time at 23 mA cm<sup>-2</sup>.

The long-term stability of an electrode is another important issue to consider for practical applications. The durability of Cu/Cu<sub>3</sub>P nanoarray-270 was examined at 23 mA cm<sup>-2</sup> in H<sub>2</sub>SO<sub>4</sub> solution, as shown in Figure 7c. The current density curve related to time reveals a minor increase after 15 h, indicating the high electrochemical stability of the Cu/Cu<sub>3</sub>P nanoarray catalysts for the HER in an acidic solution. Electrochemical impedance spectroscopy (EIS) was performed to identify the interfacial properties and catalytic kinetics of the as-synthesized Cu/Cu<sub>3</sub>P nanoarray catalyst in the HER process. As shown in Figure 7d (inset: the equivalent circuit), the series resistance values ( $R_s$ ) were obtained in the high-frequency zone, and the semicircle in the low-frequency range reflects the charge transfer resistance at the interface between the Cu/Cu<sub>3</sub>P and the electrolyte ( $R_{ct}$ ). The Nyquist plots reveal that Cu/Cu<sub>3</sub>P nanoarray-270 (4.1  $\Omega$ ) exhibits a much smaller semicircle than Cu/Cu<sub>3</sub>P nanoarray-310 (49.6  $\Omega$ ), suggesting that it has fast charge transfer kinetics for the HER. This result validates that the introduced Cu nanosheet, as a conductive substrate and nano-template, can improve the charge transport and electrochemical activity of the Cu/Cu<sub>3</sub>P nanoarray electrode.

### 3. Materials and Methods

#### 3.1. Chemicals and Materials

Copper(II) sulfate (CuSO<sub>4</sub>·5H<sub>2</sub>O), glucose (C<sub>6</sub>H<sub>12</sub>O<sub>6</sub>), polyvinylpyrrolidone (PVP,  $M_w = 30,000$ ), hydrogen peroxide (H<sub>2</sub>O<sub>2</sub>, wt% = 30%), Nafion solution and sodium hypophosphite (NaH<sub>2</sub>PO<sub>2</sub>) were purchased from Sigma-Aldrich. All chemicals were used without further purification.

#### 3.2. Synthesis of Cu Nanosheets

All chemicals in the experiment were analytical grade and used without purification. The well-defined Cu nanosheets were prepared according to the procedures in our previous

report [60]. In brief, 1.0 g  $C_6H_{12}O_6 \cdot H_2O$ , 0.5 g polyvinyl pyrrolidone (PVP) and  $CuSO_4$  were dissolved in 25 mL of deionized water with vigorous magnetic stirring, and then the mixture was transferred into a Teflon-lined autoclave and heated at 180 °C for 3 h. The brown-red products were collected, washed three times with deionized water and ethanol, respectively, and then dried in a vacuum at 60 °C.

### 3.3. Synthesis of Cu/CuO Nanoarrays

The hierarchical Cu nanosheet@CuO nanorods were synthesized by a simple hydrothermal process. In a typical synthesis procedure, an amount of Cu nanosheets and 22 mL of NaOH (0.55 mol/L) were added into a Teflon-lined vessel with vigorous magnetic stirring, and then 2 mL  $H_2O_2$  (30%) was injected rapidly into the mixture solution under stirring. Afterward, the vessel was sealed and then hydrothermally heated at 130 °C for 9 h; the as-prepared products were collected and washed three times with deionized water, and then dried in a vacuum at 60 °C.

### 3.4. Synthesis of Cu/Cu<sub>3</sub>P Nanoarrays

To prepare Cu/Cu<sub>3</sub>P nanoarrays,  $NaH_2PO_2$  was placed at the center of the tube furnace and the Cu/CuO nanoarray was placed at the downstream side of the furnace at carefully adjusted locations to set the temperature, and the distance between them was measured to be approximately 24 cm. After flushing with Ar, the center of the furnace was elevated to 270 °C with a heating rate of 2 °C/min and held at this temperature for 60 min. For comparison, samples at different phosphating temperatures were synthesized by the same process.

### 3.5. Material Characterization

XRD patterns were collected using an M21X diffractometer (MAC Science Co. Ltd., Japan) with high-intensity Cu K $\alpha$  radiation ( $\lambda = 1.541 \text{ \AA}$ ). The morphology of the products was characterized via scanning electron microscopy (SEM, ZEISS SUPRA55). The HRTEM images were collected on a FEI Tecnai F20 electron microscope operated at 200 kV. The elemental compositions and valence states of the samples were determined by XPS. XPS measurements were performed using a Thermo Fisher Scientific, Escalab-250Xi spectrometer with an Al K $\alpha$  X-ray resource. The C 1s contamination peak was used for charge correction (284.8 eV).

### 3.6. Electrochemical Measurements

The electrochemical performances of Cu/Cu<sub>3</sub>P nanoarrays were evaluated with the CHI 660D electrochemical workstation. All the electrochemical measurements were conducted in a typical three-electrode setup with an electrolyte solution of 0.5 M  $H_2SO_4$  using Cu/Cu<sub>3</sub>P nanoarrays as the working electrode, a graphite plate as the counter electrode and Ag/AgCl as the reference electrode. In all measurements, the Ag/AgCl reference electrode was calibrated with respect to a reversible hydrogen electrode (RHE). Linear sweep voltammetry (LSV) measurements were conducted in 0.5 M  $H_2SO_4$  with a scan rate of 2 mV s<sup>-1</sup>. All the potentials reported in our work were versus the RHE according to  $E_{vs. RHE} = E_{vs. Ag/AgCl} + E_{vs. Ag/AgCl}^0 + 0.059 \text{ pH}$ . Impedance measurements were carried out with a frequency range from 0.1 Hz to 10 kHz at the open-circuit potentials.

## 4. Conclusions

In summary, we have successfully prepared Cu/Cu<sub>3</sub>P nanoarrays via a facile two-step synthetic strategy, including the hydrothermal synthesis of a Cu/CuO nanoarray precursor and a low-temperature phosphorization process in an Ar atmosphere. The as-prepared Cu/Cu<sub>3</sub>P nanoarrays, as electrocatalysts, display excellent catalytic performance and durability for electrochemical hydrogen generation. Specifically, the Cu/Cu<sub>3</sub>P nanoarray-270 exhibits a low onset overpotential (96 mV) and a small Tafel slope (131 mV dec<sup>-1</sup>). The excellent electrocatalytic efficiency of the Cu/Cu<sub>3</sub>P nanoarray catalyst for the HER

can be attributed to its unique architecture. The nanoarray structure provides more active sites and contributes to the diffusion of the products. The Cu/Cu<sub>3</sub>P nanoarrays show good electrical conductivity, which is favorable to a faster transfer rate of electrons. This strategy provides an efficient technique that can be extended to other metal phosphides and metal-based nanostructures, thus creating a new opportunity in hydrogen production.

**Supplementary Materials:** The following supporting information can be downloaded at: <https://www.mdpi.com/article/10.3390/catal12070762/s1>, Figure S1: Characterization of the morphology and structure of samples: (a) SEM image of Cu nanosheet, (b) XRD patterns of Cu nanosheets, and (c) XRD patterns of Cu/CuO nanoarrays; Figure S2: The high-magnification SEM images of samples: (a,b) SEM image of Cu/CuO nanoarrays; Figure S3: The high-magnification SEM images of (a) CuO nanoplate, (b) Cu<sub>3</sub>P nanoplate; Figure S4: XPS survey spectrum of Cu /Cu<sub>3</sub>P nanoarrays; Figure S5: The SEM images and XRD patterns of samples at different phosphating time: (a,b) 1 h; (c,d) 1.5 h; Figure S6: The pure Cu nanosheet was directly phosphated and calcined: (a) SEM image; (b) XRD pattern; Table S1: Comparison of HER catalytic performance of Cu/Cu<sub>3</sub>P nanoarray-270 and other non-noble-metal electrocatalysts in acidic media.

**Author Contributions:** The manuscript was written with contributions from all authors. Conceptualization, R.D. and J.L.; methodology and investigation, R.D. and X.X.; data curation, M.X.; formal analysis, R.D. and X.X.; writing—original draft preparation, R.D.; writing—review and editing, R.D. and J.L.; visualization, M.X.; project administration, R.D. All authors have read and agreed to the published version of the manuscript.

**Funding:** This research was funded by the National Natural Science Foundation of China (Program No. 21905232) and Natural Science Basic Research Plan in Shaanxi Province of China (Program No. 2022JM-236).

**Data Availability Statement:** The data are available upon request from the corresponding author.

**Acknowledgments:** The authors thank G. Wang and H.Y. Gao (University of Science and Technology Beijing, Beijing 100083, China) and X.W. Zhang and M.Y. Han (Beijing Normal University, 100088, China) for their help.

**Conflicts of Interest:** The authors declare no conflict of interest.

## References

1. Zhang, Y.; Li, W.; Lu, L.; Song, W. Tuning active sites on cobalt/nitrogen doped graphene for electrocatalytic hydrogen and oxygen evolution. *Electrochim. Acta* **2018**, *265*, 497–506. [CrossRef]
2. Jebaslinhepzybai, B.T.; Prabu, N.; Sasidharan, M. Facile galvanic replacement method for porous nanoparticles as an efficient HER electrocatalyst. *Int. J. Hydrog. Energy* **2020**, *45*, 11127–11137. [CrossRef]
3. Jiang, H.; Gu, J.; Zheng, X.; Liu, M.; Qiu, X.; Wang, L.; Li, W.; Chen, Z.; Ji, X.; Li, J. Defect-rich and ultrathin N doped carbon nanosheets as advanced trifunctional metal-free electrocatalysts for the ORR, OER and HER. *Energy Environ. Sci.* **2019**, *12*, 322–333. [CrossRef]
4. Li, Y.; Liu, J.; Chen, C.; Zhang, X.; Chen, J. Preparation of NiCoP Hollow Quasi-Polyhedra and Their Electrocatalytic Properties for Hydrogen Evolution in Alkaline Solution. *ACS Appl. Mater. Interfaces* **2017**, *9*, 5982–5991. [CrossRef]
5. Martini, B.K.; Maia, G. Using a combination of Co, Mo, and Pt oxides along with graphene nanoribbon and MoSe<sub>2</sub> as efficient catalysts for OER and HER. *Electrochim. Acta* **2021**, *391*, 138907. [CrossRef]
6. Yu, J.; Dai, Y.; He, Q.; Cheng, C.; Ni, M. Robust non-Pt noble metal-based nanomaterials for electrocatalytic hydrogen generation. *Appl. Phys. Rev.* **2020**, *7*, 041304. [CrossRef]
7. El-Hallag, I.; Elsharkawy, S.; Hammad, S. The effect of electrodeposition potential on catalytic properties of Ni nanoparticles for hydrogen evolution reaction (HER) in alkaline media. *J. Appl. Electrochem.* **2022**, *52*, 907–918. [CrossRef]
8. Li, Y.; Wang, H.; Xie, L.; Liang, Y.; Hong, G.; Dai, H. MoS<sub>2</sub> Nanoparticles Grown on Graphene: An Advanced Catalyst for Hydrogen Evolution Reaction. *J. Am. Chem. Soc.* **2011**, *133*, 7296–7299. [CrossRef]
9. Popczun, E.J.; Mckone, J.R.; Read, C.G.; Biacchi, A.J.; Wiltout, A.M.; Lewis, N.S.; Schaak, R.E. Nanostructured nickel phosphide as an electrocatalyst for the hydrogen evolution reaction. *J. Am. Chem. Soc.* **2013**, *135*, 9267–9270. [CrossRef]
10. Li, S.; Wang, Y.; Wang, H.; Zhang, Q.; Zhang, Z.; Liu, H. Correction to: Heterostructures of MXenes and CoNx-Graphene as highly active electrocatalysts for hydrogen evolution reaction in alkaline media. *J. Appl. Electrochem.* **2021**, *51*, 1109. [CrossRef]
11. Pu, M.; Wang, D.; Zhang, Z.; Guo, Y.; Guo, W. Flexoelectricity enhanced water splitting and hydrogen evolution reaction on grain boundaries of monolayer transition metal dichalcogenides. *Nano Res.* **2022**, *15*, 978–984. [CrossRef]

12. Pak, S.; Lim, J.; Hong, J.; Cha, S.N. Enhanced Hydrogen Evolution Reaction in Surface Functionalized MoS<sub>2</sub> Monolayers. *Catalysts* **2021**, *11*, 70. [[CrossRef](#)]
13. Yan, X.; Huang, S.; Yang, F.; Sun, S.; Li, Y. Enhanced Catalytic Hydrogen Evolution Reaction Performance of Highly Dispersed Ni<sub>2</sub>P Nanoparticles Supported by P-Doped Porous Carbon. *Colloids Surf. A Physicochem. Eng. Asp.* **2021**, *616*, 126308. [[CrossRef](#)]
14. Kluge, R.M.; Haid, R.W.; Stephens, I.; Callevallejo, F.; Bandarenka, A.S. Monitoring the active sites for the hydrogen evolution reaction at model carbon surfaces. *Phys. Chem. Chem. Phys.* **2021**, *23*, 10051–10058. [[CrossRef](#)]
15. Kita, H.; Shen, Y.; Gao, Y. Mass transfer effect in hydrogen evolution reaction on Pt single-crystal electrodes in acid solution. *J. Electroanal. Chem.* **1992**, *334*, 351–357. [[CrossRef](#)]
16. Yang, B.; Xu, J.; Duan, B.; Wang, J.; Liu, B. Amorphous phosphatized ruthenium-iron bimetallic nanoclusters with Pt-like activity for hydrogen evolution reaction. *Appl. Catal. B Environ.* **2021**, *283*, 119583. [[CrossRef](#)]
17. Lai, Y.; Zhang, Z.; Tan, Y.; Yu, L.; Wu, W.; Wang, Z.; Jiang, T.; Gao, S.; Cheng, N. Electronic modulation of Pt nanoclusters through tuning the interface of Pt-SnO<sub>2</sub> clusters for enhanced hydrogen evolution catalysis. *Chem. Eng. J.* **2022**, *435*, 135102. [[CrossRef](#)]
18. Chen, J.; Chen, C.; Chen, Y.; Wang, H.; Wang, Y. Improving alkaline hydrogen evolution reaction kinetics on molybdenum carbide: Introducing Ru dopant. *J. Catal.* **2020**, *392*, 313–321. [[CrossRef](#)]
19. Cai, J.; Liao, X.; Li, P.; Wang, Q.; Huang, H.; Lyu, Z.; Lin, J.; Xie, S. Penta-Twinned Rh@Pt Core-Shell nanobranches with engineered shell thickness for reversible and active hydrogen redox electrocatalysis. *Chem. Eng. J.* **2022**, *429*, 132414. [[CrossRef](#)]
20. Yang, Q.; Li, G.; Manna, K.; Fan, F.; Sun, Y. Topological Engineering of Pt-Group-Metal-Based Chiral Crystals toward High-Efficiency Hydrogen Evolution Catalysts. *Adv. Mater.* **2020**, *32*, 1908518. [[CrossRef](#)]
21. Jy, A.; Dan, W.B.; Zhe, Z.B.; Wy, A.; Hs, A.; Yq, A.; Sw, B.; Yukc, D.; Yz, C. Facile synthesis of Nafion-supported Pt nanoparticles with ultra-low loading as a high-performance electrocatalyst for hydrogen evolution reaction. *J. Colloid Interface Sci.* **2020**, *566*, 505–512.
22. Tiwari, J.N.; Dang, N.K.; Sultan, S.; Thangavel, P.; Jeong, H.Y.; Kim, K.S. Multi-heteroatom-doped carbon from waste-yeast biomass for sustained water splitting. *Nat. Sustain.* **2020**, *3*, 556–563. [[CrossRef](#)]
23. Bae, S.Y.; Mahmood, J.; Jeon, I.Y.; Baek, J.B. Recent advances in ruthenium-based electrocatalysts for the hydrogen evolution reaction. *Nanoscale Horiz.* **2020**, *5*, 43–56. [[CrossRef](#)]
24. Bonde, J.; Moses, P.G.; Jaramillo, T.F.; Nørskov, J.K.; Chorkendorff, I. Hydrogen evolution on nano-particulate transition metal sulfides. *Faraday Discuss.* **2008**, *140*, 219–231. [[CrossRef](#)]
25. Reeve, R.W.; Christensen, P.A.; Dickinson, A.J.; Hamnett, A.; Scott, K. Methanol-tolerant oxygen reduction catalysts based on transition metal sulfides and their application to the study of methanol permeation. *Electrochim. Acta* **2000**, *45*, 4237–4250. [[CrossRef](#)]
26. Ys, A.; Ch, B.; Js, A.; Yz, A.; Jn, C.; Yong, H.A. One-step construction of a transition-metal surface decorated with metal sulfide nanoparticles: A high-efficiency electrocatalyst for hydrogen generation. *J. Colloid Interface Sci.* **2020**, *558*, 1–8.
27. Dolmatov, V.S.; Kuznetsov, S.A. Synthesis of Refractory Metal Carbides on Carbon Fibers in Molten Salts and Their Electrocatalytic Properties. *J. Electrochem. Soc.* **2021**, *168*, 122501. [[CrossRef](#)]
28. Díaz-Coello, S.; Afonso, M.M.; Palenzuela, J.A.; Pastor, E.; García, G. Composite materials from transition metal carbides and ionic liquids as electrocatalyst for hydrogen evolution in alkaline media. *J. Electroanal. Chem.* **2021**, *898*, 115620. [[CrossRef](#)]
29. Ihsanullah, I. MXenes (two-dimensional metal carbides) as emerging nanomaterials for water purification: Progress, challenges and prospects. *Chem. Eng. J.* **2020**, *388*, 124340. [[CrossRef](#)]
30. Yu, F.; Zhang, X.; Yang, Z.; Yang, P.; Ma, J. Environmental applications of two-dimensional transition metal carbides and nitrides for water purification: A review. *Environ. Chem. Lett.* **2022**, *20*, 633–660. [[CrossRef](#)]
31. Yan-Juan, L.I.; Wang, M.; Liu, S.; Gao, J.X.; Yan, X. Preparation and properties of transition metal nitrides caged in N-doped hollow porous carbon sphere for oxygen reduction reaction. *Trans. Nonferrous Met. Soc. China* **2021**, *31*, 1427–1438.
32. Sun, H.; Yan, Z.; Liu, F.; Xu, W.; Cheng, F.; Chen, J. Self-Supported Transition-Metal-Based Electrocatalysts for Hydrogen and Oxygen Evolution. *Adv. Mater.* **2020**, *32*, 1806326.1–1806326.18. [[CrossRef](#)]
33. Li, A.; Zhang, L.; Wang, F.; Li, L.; Chen, H.; Wei, Z. Rational design of porous Ni-Co-Fe ternary metal phosphides nanobricks as bifunctional electrocatalysts for efficient overall water splitting. *Appl. Catal. B Environ.* **2022**, *310*, 121353. [[CrossRef](#)]
34. Han, P.; Li, B.; Dang, Y.; Zhou, Y. A Novel Trimetal Phosphide with Amorphous Porous Structure for the Enhanced Electrocatalysis of Oxygen Evolution Reaction. *J. Electrochem. Soc.* **2021**, *168*, 116510.
35. Wy, A.; Yg, A.; Zhi, C.A.; Ying, Z.A.; Zw, A.; Lei, W. Strategies on improving the electrocatalytic hydrogen evolution performances of metal phosphides. *Chin. J. Catal.* **2021**, *42*, 1876–1902.
36. Liu, L.; Li, N.; Han, J.; Yao, K.; Liang, H. Multicomponent transition metal phosphide for oxygen evolution. *Int. J. Miner. Metall. Mater.* **2022**, *29*, 503–512. [[CrossRef](#)]
37. Jian, L.; Gao, X.; Liu, B.; Feng, Q.; Li, X.B.; Huang, M.Y.; Liu, Z.; Zhang, J.; Tung, C.H.; Wu, L.Z. Graphdiyne: A Metal-Free Material as Hole Transfer Layer to Fabricate Quantum Dot-Sensitized Photocathodes for Hydrogen Production. *J. Am. Chem. Soc.* **2016**, *138*, 3954.
38. Cao, R.; Hu, F.; Zhang, T.; Shao, W.; Jian, X. Bottom-up fabrication of triazine-based frameworks as metal-free materials for supercapacitors and oxygen reduction reaction. *RSC Adv.* **2021**, *11*, 8384–8393. [[CrossRef](#)]
39. Wei, S.; Qi, K.; Jin, Z.; Cao, J.; Zheng, W.; Chen, H.; Cui, X. One-Step Synthesis of a Self-Supported Copper Phosphide Nanobush for Overall Water Splitting. *ACS Omega* **2016**, *1*, 1367–1373. [[CrossRef](#)]

40. Ping, L.; Rodriguez, J.A. Catalysts for hydrogen evolution from the [NiFe] hydrogenase to the Ni<sub>2</sub>P (001) surface: The importance of ensemble effect. *J. Am. Chem. Soc.* **2005**, *127*, 14871–14878.
41. Zhang, W.; Hong, J.; Zheng, J.; Huang, Z.; Zhou, J.; Xu, R. Nickel-thiolate complex catalyst assembled in one step in water for solar H<sub>2</sub> production. *J. Am. Chem. Soc.* **2011**, *133*, 20680–20683. [[CrossRef](#)]
42. Li, Q.; Xing, Z.; Asiri, A.M.; Ping, J.; Sun, X. Cobalt phosphide nanoparticles film growth on carbon cloth: A high-performance cathode for electrochemical hydrogen evolution. *Int. J. Hydrog. Energy* **2014**, *39*, 16806–16811. [[CrossRef](#)]
43. Cao, S.; Yong, C.; Wang, C.J.; He, P.; Fu, W.F. Highly efficient photocatalytic hydrogen evolution by nickel phosphide nanoparticles from aqueous solution. *Chem. Commun.* **2014**, *50*, 10427–10429. [[CrossRef](#)]
44. Mcenaney, J.M.; Crompton, J.C.; Callejas, J.F.; Popczun, E.J.; Biacchi, A.J.; Lewis, N.S.; Schaak, R.E. Amorphous Molybdenum Phosphide Nanoparticles for Electrocatalytic Hydrogen Evolution. *Chem. Mater.* **2014**, *26*, 4826–4831. [[CrossRef](#)]
45. Wu, Y.; Li, Y.; Yuan, M.; Zhe, L.; Wei, B. Direct growth of Ni–Fe phosphides nanohybrids on NiFe foam for highly efficient water oxidation. *J. Alloys Compd.* **2020**, *847*, 156363. [[CrossRef](#)]
46. You, B.; Jiang, N.; Sheng, M.; Bhushan, M.W.; Sun, Y. Hierarchically Porous Urchin-Like Ni<sub>2</sub>P Superstructures Supported on Nickel Foam as Efficient Bifunctional Electrocatalysts for Overall Water Splitting. *ACS Catal.* **2016**, *6*, 714–721. [[CrossRef](#)]
47. Gao, X.; Lu, K.; Chen, J.; Min, J.; Tan, M. NiCoP–CoP heterostructural nanowires grown on hierarchical Ni foam as a novel electrocatalyst for efficient hydrogen evolution reaction. *Int. J. Hydrog. Energy* **2021**, *46*, 23205–23213. [[CrossRef](#)]
48. Yang, Z.; Tuo, Y.; Lu, Q.; Chen, C.; Liu, M.; Liu, B.; Duan, X.; Zhou, Y.; Zhang, J. Hierarchical Cu<sub>3</sub>P-based nanoarrays on nickel foam as efficient electrocatalysts for overall water splitting. *Green Energy Environ.* **2020**, *2*, 236–245. [[CrossRef](#)]
49. Hou, C.C.; Chen, Q.Q.; Wang, C.J.; Liang, F.; Lin, Z.; Fu, W.F.; Chen, Y. Self-Supported Cedarlike Semimetallic Cu<sub>3</sub>P Nanoarrays as a 3D High-Performance Janus Electrode for Both Oxygen and Hydrogen Evolution under Basic Conditions. *ACS Appl. Mater. Interfaces* **2016**, *8*, 23037–23048. [[CrossRef](#)]
50. Shiri, P. An overview on the copper-promoted synthesis of five-membered heterocyclic systems. *Appl. Organomet. Chem.* **2020**, *34*, 5600–5622. [[CrossRef](#)]
51. Zheng, H.; Huang, X.; Gao, H.; Lu, G.; Dong, W.; Wang, G. Cu@Cu<sub>3</sub>P core-shell nanowires attached on Ni foam as high-performance electrocatalyst for hydrogen evolution reaction. *Chemistry* **2018**, *25*, 1083–1089. [[PubMed](#)]
52. Fedorov, A.; Saraev, A.; Kremneva, A.; Selivanova, A.; Vorokhta, M.; Šmíd, B.; Bulavchenko, O.; Yakovlev, V.; Kaichev, V. Kinetic and mechanistic study of CO oxidation over nanocomposite CuFeAl oxide catalysts. *ChemCatChem* **2020**, *19*, 4911–4921. [[CrossRef](#)]
53. Rong, J.; Xu, J.; Qiu, F.; Zhu, Y.; Fang, Y.; Xu, J.; Zhang, T. Sea Urchin-Like MOF-Derived Formation of Porous Cu<sub>3</sub>P@C as an Efficient and Stable Electrocatalyst for Oxygen Evolution and Hydrogen Evolution Reactions. *Adv. Mater. Interfaces* **2019**, *6*, 1900502. [[CrossRef](#)]
54. Zhou, X.; Zhou, X.; Liu, L.; Chen, H.; Hu, X.; Qian, J.; Huang, D.; Zhang, B.; Tang, J. Self-supported Cu<sub>3</sub>P nanowire electrode as an efficient electrocatalyst for the oxygen evolution reaction. *RSC Adv.* **2021**, *11*, 34137–34143. [[CrossRef](#)] [[PubMed](#)]
55. Kou, Y.; Wang, K.; Wumaer, M.; Guo, C.; Tian, B.; Zhang, L.; Akram, N.; Wang, J. Synthesis of hollow Cu@Cu<sub>3-x</sub>P core-shell nanostructure as dual-functional catalyst with copper vacancy for enhancing chemical reduction and photocatalytic performance. *Appl. Surf. Sci.* **2022**, *589*, 153031. [[CrossRef](#)]
56. Ma, L.; Shen, X.; Zhou, H.; Zhu, J.; Xi, C.; Ji, Z.; Kong, L. Synthesis of Cu<sub>3</sub>P nanocubes and their excellent electrocatalytic efficiency for the hydrogen evolution reaction in acidic solution. *RSC Adv.* **2016**, *6*, 9672–9677. [[CrossRef](#)]
57. Tian, J.; Liu, Q.; Cheng, N.; Asiri, A.M.; Sun, X. Self-supported Cu<sub>3</sub>P nanowire arrays as an integrated high-performance three-dimensional cathode for generating hydrogen from water. *Angew. Chem.* **2015**, *126*, 9731–9735. [[CrossRef](#)]
58. Tian, T.; Ai, L.; Jiang, J. Metal–organic framework-derived nickel phosphides as efficient electrocatalysts toward sustainable hydrogen generation from water splitting. *RSC Adv.* **2015**, *5*, 10290–10295. [[CrossRef](#)]
59. Xu, Y.; Wu, R.; Zhang, J.; Shi, Y.; Zhang, B. Anion-exchange synthesis of nanoporous FeP nanosheets as electrocatalysts for hydrogen evolution reaction. *Chem. Commun.* **2013**, *49*, 6656–6658. [[CrossRef](#)]
60. Dang, R.; Song, L.L.; Dong, W.J.; Li, C.R.; Zhang, X.B. Synthesis and self-assembly of large-area Cu nanosheets and their application as an aqueous conductive ink on flexible electronics. *ACS Appl. Mater. Interfaces* **2014**, *6*, 622–629. [[CrossRef](#)]